



NRL/MR/6110--08-9155

EM61-MK2 Response of Standard Munitions Items

H.H. NELSON

*Chemical Dynamics and Diagnostics Branch
Chemistry Division*

T. BELL

J. KINGDON

N. KHADR

*SAIC, Inc.
Arlington, Virginia*

D.A. STEINHURST

*Nova Research, Inc.
Alexandria, Virginia*

October 6, 2008

Approved for public release; distribution is unlimited.

REPORT DOCUMENTATION PAGE

Form Approved
OMB No. 0704-0188

Public reporting burden for this collection of information is estimated to average 1 hour per response, including the time for reviewing instructions, searching existing data sources, gathering and maintaining the data needed, and completing and reviewing this collection of information. Send comments regarding this burden estimate or any other aspect of this collection of information, including suggestions for reducing this burden to Department of Defense, Washington Headquarters Services, Directorate for Information Operations and Reports (0704-0188), 1215 Jefferson Davis Highway, Suite 1204, Arlington, VA 22202-4302. Respondents should be aware that notwithstanding any other provision of law, no person shall be subject to any penalty for failing to comply with a collection of information if it does not display a currently valid OMB control number. **PLEASE DO NOT RETURN YOUR FORM TO THE ABOVE ADDRESS.**

1. REPORT DATE (DD-MM-YYYY) 06-10-2008		2. REPORT TYPE Interim		3. DATES COVERED (From - To) February 2008 – August 2008	
4. TITLE AND SUBTITLE EM61-MK2 Response of Standard Munitions Items				5a. CONTRACT NUMBER W74RDV73544541	
				5b. GRANT NUMBER	
				5c. PROGRAM ELEMENT NUMBER	
6. AUTHOR(S) H.H. Nelson, T. Bell,* J. Kingdon,* N. Khadr,* and D.A. Steinhurst†				5d. PROJECT NUMBER	
				5e. TASK NUMBER	
				5f. WORK UNIT NUMBER 61-5802-S-8	
7. PERFORMING ORGANIZATION NAME(S) AND ADDRESS(ES) Naval Research Laboratory, Code 6110 4555 Overlook Avenue, SW Washington, DC 20375-5320				8. PERFORMING ORGANIZATION REPORT NUMBER NRL/MR/6110--08-9155	
9. SPONSORING / MONITORING AGENCY NAME(S) AND ADDRESS(ES) Environmental Security Technology Certification Program 901 North Stuart Street, Suite 303 Arlington, VA 22203				10. SPONSOR / MONITOR'S ACRONYM(S) ESTCP	
				11. SPONSOR / MONITOR'S REPORT NUMBER(S)	
12. DISTRIBUTION / AVAILABILITY STATEMENT Approved for public release; distribution is unlimited.					
13. SUPPLEMENTARY NOTES *SAIC, Inc., Arlington, VA 22202 †Nova Research, Inc., Alexandria, VA 22308					
14. ABSTRACT Target response coefficients for 13 commonly encountered UXO items were calculated from measurements made using the recently developed NRL Time-domain Electromagnetic Induction array. These response coefficients were used to predict the signals expected from an EM61-MK2, the most commonly used geophysical survey instrument for UXO, for each of these items as a function of orientation and distance of the center of the item below the bottom coil of the sensor. A series of EM61-MK2 survey measurements were made over the object at the NRL Blossom Point Test site to confirm the predictions. These predicted EM61-MK2 signals are presented graphically with the confirming survey measurements plotted on the same axes. The minimum signal at each of the four gates available from the EM61-MK2 is tabulated for a depth corresponding to 11× the object's diameter, the de facto expectation for detectability with modern geophysical equipment, and all the results obtained are attached electronically as a spreadsheet.					
15. SUBJECT TERMS Unexploded ordnance (UXO) Electromagnetic induction (EMI)					
16. SECURITY CLASSIFICATION OF:			17. LIMITATION OF ABSTRACT	18. NUMBER OF PAGES	19a. NAME OF RESPONSIBLE PERSON
a. REPORT	b. ABSTRACT	c. THIS PAGE			Herbert H. Nelson
Unclassified	Unclassified	Unclassified	UL	29	19b. TELEPHONE NUMBER (include area code) (202) 767-3686

CONTENTS

FIGURES	iv
TABLES	v
INTRODUCTION.....	1
DESCRIPTION OF THE MODEL	2
DATA COLLECTION PROCEDURES	7
RESULTS.....	9
SUMMARY	23
REFERENCES.....	24
APPENDIX A – Tabulated Results.....	attached electronically

FIGURES

Figure 1 – Step response and effective β s for a 3” chrome steel and a 4” aluminum sphere	5
Figure 2 – Predicted EM61-MK2 signal at the second time gate as a function of depth for a 105-mm projectile and a 2.75” rocket warhead.....	6
Figure 3 – Schematic of the 25-element TEM array used to determine the response coefficients of the test objects.....	7
Figure 4 – 81-mm mortar placed under the TEM array.....	7
Figure 5 – Measured response of a 2.75-in warhead oriented horizontally along track 35 cm below the TEM array.....	8
Figure 6 – EM61-MK2 signal at the second time gate as a function of distance below the sensor for a 155-mm projectile.....	10
Figure 7 – EM61-MK2 signal at the second time gate as a function of distance below the sensor for a 4.2-in mortar	11
Figure 8 – EM61-MK2 signal at the second time gate as a function of distance below the sensor for a 105-mm projectile.....	12
Figure 9 – EM61-MK2 signal at the second time gate as a function of distance below the sensor for a 105-mm HEAT projectile	13
Figure 10 – EM61-MK2 signal at the second time gate as a function of distance below the sensor for a 81-mm mortar.....	14
Figure 11 – EM61-MK2 signal at the second time gate as a function of distance below the sensor for a 3-in Stokes mortar	15
Figure 12 – EM61-MK2 signal at the second time gate as a function of distance below the sensor for a 75-mm projectile	16
Figure 13 – EM61-MK2 signal at the second time gate as a function of distance below the sensor for a 2.75-in rocket warhead.....	17
Figure 14 – EM61-MK2 signal at the second time gate as a function of distance below the sensor for a 2.36-in Rocket Propelled Grenade	18
Figure 15 – EM61-MK2 signal at the second time gate as a function of distance below the sensor for a 60-mm mortar.....	19
Figure 16 – EM61-MK2 signal at the second time gate as a function of distance below the sensor for a 40-mm grenade.....	20
Figure 17 – EM61-MK2 signal at the second time gate as a function of distance below the sensor for a 37-mm projectile	21

Figure 18 – EM61-MK2 signal at the second time gate as a function of distance below the sensor for a hand grenade..... 22

TABLES

Table 1. Nominal delay time and receive coil used for each of the EM61-MK2 gates in “D” mode..... 8

Table 2. Measured RMS noise for each of the four gates in static and survey mode. 9

Table 3. Predicted minimum EM61-MK2 signal at each gate for a variety of munitions at a depth corresponding to 11x their respective diameter 23

EM61-MK2 RESPONSE OF STANDARD MUNITIONS ITEMS

INTRODUCTION

The EM61-MK2 Electromagnetic Induction sensor (Geonics Limited, Mississauga, Ontario, Canada) is the most widely used geophysical sensor for unexploded ordnance (UXO) detection surveys. Like all time-domain electromagnetic induction sensors, it produces a pulsed magnetic field (primary field) that induces a secondary field in metallic objects in the vicinity of the sensor. The decay of this induced field is sensed by monitoring the current in a wire-loop receiver coil in four time gates after the turn-off of the primary field. In the EM61-MK2, the main receiver coil is co-located with the transmit coil.

In a typical UXO detection survey, the sensor, with attached wheels or mounted on a cart, is used to survey the field in a raster pattern with a line spacing on the order of the 1-m width of the sensor. Smaller line spacings can be used to increase the data density for more advanced analyses. After data collection, the raw data are typically leveled, background corrected, and mapped. Then, either line-by-line or from a data image, regions of anomalous response are selected and marked as potential metal targets. This initial list of anomalies is used as input to an analysis step that selects anomalies for digging based on features extracted during further analyses such as target size and shape.

There are two schools of thought on how best to select anomalies for the initial list. The goal, of course, is to remove all hazardous objects from the field so one would like to ensure that the initial list includes all hazardous objects. The first approach is to select all points with sensor readings above some multiple of the survey noise as anomalies. In some cases, this threshold can be as low as 1.5x the sensor noise, which can lead to a very long anomaly list. This approach is intended to maximize the likelihood that all items of interest (unexploded ordnance and residual high explosive material in this case) are included on the anomaly list. By definition, however, it includes a number of items with low signal-to-noise ratio (SNR); $SNR = 1.5$ in the case described above. It is difficult to extract usable target features from signals with such low SNR so, even if there is a subsequent analysis and classification step, one will often not be able to remove these targets from the dig list, they will have to be dug. But, the average cost of a dig on a munitions site can be up to \$125 when the cost of the trained personnel and safety procedures required is factored in. So, the approach that maximizes the number of initial anomalies selected with low SNR can lead to a very expensive remediation; often more than the available resources.

Another approach, which we and others have advocated, is to consider the possible sensor response of the targets of interest when setting the threshold for anomaly selection. In this approach, one would model the signal expected for each of the targets of interest and set the threshold at the smallest sensor reading expected from the smallest target of interest at its maximum depth. Even with a safety factor applied to the sensor reading specified above, this method often leads to a higher anomaly selection threshold than the traditional approach. The implication of this is that anomalies due to potential metal objects are left un-remediated but we are confident that the objects responsible for the anomaly have a smaller response than any of our targets of interest. This approach to anomaly selection was used at the recent Environmental Security Technology Certification Program (ESTCP) Discrimination Study at former Camp Sibert, AL with no targets of interest missed [1].

To implement this target-of-interest based threshold method one must be able to confidently predict the sensor response of all possible items of interest as a function of depth. This is a relatively straight forward process for the EM61-MK2 sensor. Over the past ten years we have been involved in a number of programs supported by ESTCP in which we have collected data using variants of the EM61-MK2, developed models to interpret those data, and participated in blind tests to validate our procedures.

In this report, we use these models to predict the response of an EM61-MK2 to a number of common munitions as a function of depth. To validate the results, we have collected survey data over these same objects at varying depths and orientations, extracted the maximum signal observed, and compared the measurements to our predictions. In all cases, the model accurately predicts the measured anomaly amplitudes. After a brief description of the model employed and the data collection methodology, we present the predicted and measured anomaly data in graphical and tabular form.

DESCRIPTION OF THE MODEL

The response of a metallic object to an Electromagnetic Induction sensor is most simply modeled as an induced dipole moment represented by a magnetic polarizability matrix \mathbf{B} [2]. As a consequence of electromagnetic reciprocity, the matrix \mathbf{B} is symmetric. By a suitable rotation it can be transformed to diagonal form, so we can write

$$\mathbf{B} = \mathbf{U}\mathbf{B}_0\mathbf{U}^T \quad (1)$$

with

$$\mathbf{B}_0 = \begin{bmatrix} \beta_1 & 0 & 0 \\ 0 & \beta_2 & 0 \\ 0 & 0 & \beta_3 \end{bmatrix}. \quad (2)$$

In terms of yaw, pitch and roll Euler angles ϕ , θ and ψ [3], the rotation matrix \mathbf{U} is given by

$$\mathbf{U} = \begin{bmatrix} \cos \theta \cos \phi & \cos \theta \sin \phi & -\sin \theta \\ \sin \psi \sin \theta \cos \phi - \cos \psi \sin \phi & \sin \psi \sin \theta \sin \phi + \cos \psi \cos \phi & \cos \theta \sin \psi \\ \cos \psi \sin \theta \cos \phi + \sin \psi \sin \phi & \cos \psi \sin \theta \sin \phi - \sin \psi \cos \phi & \cos \theta \cos \psi \end{bmatrix}. \quad (3)$$

The eigenvalues β_1 , β_2 , β_3 correspond to responses induced by the sensor transmit field components aligned with each of the object's principal axes. ϕ , θ and ψ together define the orientations of these principal axes relative to the X, Y and Z coordinate directions. Depending on sensor modality, the β s are functions either of time after the primary field cutoff or of the frequency of the primary field; the Euler angles are not.

In terms of \mathbf{B} above, the time-domain EMI sensor signal S is modeled as

$$S(t) = \mu_0 A I_0 \mathbf{C}_R \cdot \mathbf{C}_T \left\{ \frac{d}{dt} \int \hat{I}(t - \tau) \mathbf{B}(\tau) d\tau \right\} \equiv \mu_0 A I_0 \mathbf{C}_R \cdot \mathbf{C}_T \mathbf{B}_E(t) \quad (4)$$

In equation (4), μ_0 is the magnetic permeability of free space ($4\pi \times 10^{-7}$ volt-sec/amp-m); A is a scaling factor that depends on the number of turns in the transmit and receive coils, the receiver gain, etc.; I_0 is the peak amplitude of the transmit current pulse; \mathbf{C}_T and \mathbf{C}_R are coil sensitivity functions for the transmit and receive coils; and \mathbf{B}_E is the effective polarizability matrix, a quantity which encapsulates the influence of the normalized transmit pulse $\hat{I}(t)$ on \mathbf{B} . \mathbf{C}_T and \mathbf{C}_R depend only on coil geometry and location relative to the object, while \mathbf{B} depends only on what the object is and how it's oriented, not where it is. The coil sensitivity functions are vectors that specify (a) the strength and direction of the primary field at the object (\mathbf{C}_T) and (b) the sensitivity of the receive coil to the vector components of a magnetic dipole source at the object location (\mathbf{C}_R). The vector $\mathbf{C}_T \mathbf{B}_E$ describes the strength of the induced object response in the X, Y and Z coordinate directions. Taking the dot product with \mathbf{C}_R accounts for the relative sensitivity of the receive coil to each of these response components.

The strength and direction of \mathbf{C}_T and \mathbf{C}_R are sensitive functions of the location of the EMI sensor relative to the object. \mathbf{C}_T and \mathbf{C}_R are defined in terms of integrals around the coil involving the vector from the object to the coil:

$$\mathbf{C}_{T,R}(\mathbf{r}_0) = \frac{1}{4\pi} \oint_{T,R} \frac{d\mathbf{l} \times (\mathbf{r}_0 - \mathbf{r})}{|\mathbf{r}_0 - \mathbf{r}|^3} \quad (5)$$

where \mathbf{r}_0 is the location of the object and \mathbf{r} is the location of a point on the coil.

The effective polarizability matrix \mathbf{B}_E , as expressed in (4), makes explicit reference to the filtering of \mathbf{B} via the transmit pulse. However, in general, the situation may further be complicated by the effects of the receiver electronics, which also filter the response. In practice, the latter is accounted for by lumping an object-dependent scale factor into \mathbf{B}_E and using standard test objects to calibrate the sensor by determining A . The eigenvalues (i.e. β s) of the effective polarizability matrix thus become the quantities which we work with.

In general, the aggregate magnitude of the β s determines the size of the object, while differences among the β s relates to the shape of the object. For axially symmetric shapes such as cylinders, prolate or oblate spheroids, and many UXO items, there is a basic longitudinal response along its length and two equal responses transverse to this.

Deriving the β s from EMI data collected over an object is fairly straightforward. As the sensor moves relative to the object, the object is excited from different directions, while the sensitivity of the receiver to the different response components also varies – data from different locations above the object combine the elements of the polarizability matrix \mathbf{B}_E in different ways. As it turns out, if enough data are collected over an area whose dimensions are somewhat larger than the depth of the object, then all of the elements in \mathbf{B}_E contribute enough, and in enough different ways to the overall response that the data can be inverted to determine the β s.

With data collected at N locations ($\mathbf{r}_i, i=1,2,\dots,N$) over an unknown object, we have an overdetermined set of N simultaneous equations with nine unknown quantities (three β s, three Euler angles that define the object's orientation, and the xyz coordinates of the unknown target location \mathbf{r}_0):

$$S_i = \mu_0 A I_0 \mathbf{C}_R(\mathbf{r}_0 - \mathbf{r}_i) \cdot \mathbf{C}_T(\mathbf{r}_0 - \mathbf{r}_i) \mathbf{B}_E, \quad i=1,2,\dots,N. \quad (6)$$

The equations are solved in a least-squares sense simultaneously for all values of time. This is accomplished by using a Levenberg-Marquardt gradient search technique to determine the target parameters that minimize the mean squared error between the dipole response model and the measured data.

A key assumption of the dipole response model outlined above is that the behavior with time of the induced currents within an object – from the early surface currents to the later volume currents – is fully embodied in \mathbf{B} (and hence the β s) defined *at a single point in space*. For the case of a simple compact object sufficiently far from the sensor, this is a very good approximation and can be represented by a unique set of β s. For the case of composite and/or extended objects sufficiently far from the sensor, the model can still give a reasonably good approximation but must now be represented by different sets of β s that depend on the object orientation relative to the sensor.

Note from (4) that for the special case where $\hat{I}(t)$ is an ideal step function, $\mathbf{B}_E \equiv \mathbf{B}$ for all time t after the transition from one to zero occurs. For this reason, we refer to the β s from \mathbf{B} as the *step response* β s and the β s from \mathbf{B}_E as the *effective* β s. Figure 1 below shows plots of the step response and effective β s for a 3” chrome steel and a 4” aluminum sphere. The underlying black curves in each panel represent the step response β s as obtained from theory. Since the sphere is perfectly symmetric, $\beta_1=\beta_2=\beta_3$. Overplotted in green are the theoretical effective β s for our TEM array (described in the next section) computed solely by convolving the TEM transmit pulse with the step response β s followed by the time derivative, as prescribed by (4). The effective β s derived directly from data taken with the TEM array are shown in red. In this case, the β s (solid, dotted and dashed curves) are essentially identical, as expected. Note that for both the ferrous and nonferrous spheres, the derived effective β s from the TEM array data are an extremely good representation of the step response β s.

For comparison, the magenta curves show the theoretical effective β s for the EM61-MK2. These are computed again as prescribed by (4), but now the pulse being used is that of the EM61-MK2. Note that in this case, the derived effective β s are generally not a good representation of the step response β s. Coincidentally, however, in the regime of the EM61-MK2 time gates (shown as vertical dotted lines), the 3” chrome steel sphere β s are an approximate representation of the step response β s.

Since the EM61-MK2 signal vs depth curves in this report are generated via (4), and step response β s are given as derived from the TEM array data, it will be necessary to accurately convert these to effective β s for the EM61-MK2. A method which appears successful involves fitting each red curve with the sum of a weighted arbitrary number of loops using a procedure developed in SERDP project MM-1313 [4,5]. The cyan curves represent the result of convolving these fitted curves with the EM61-MK2 transmit pulse and taking the time derivative, as prescribed by (4).

Two examples of the predicted EM61-MK2 response in gate 2 are shown in Figure 2. The left panel plots the response expected from a 105mm projectile while the right panel plots the response expected from a 2.75” rocket warhead. For both cases, the predicted responses are plotted as a function of the distance of the items center below the bottom coil of the sensor. In normal operation, the EM61-MK2 is deployed on wheels with the bottom coil 42 cm off the ground. For this case, the target depth below the ground will equal the abscissa reading minus 42 cm. Other deployment schemes have the EM61-MK2 sensors mounted on trays that are dragged across the ground. In those cases, a different offset would be applied.

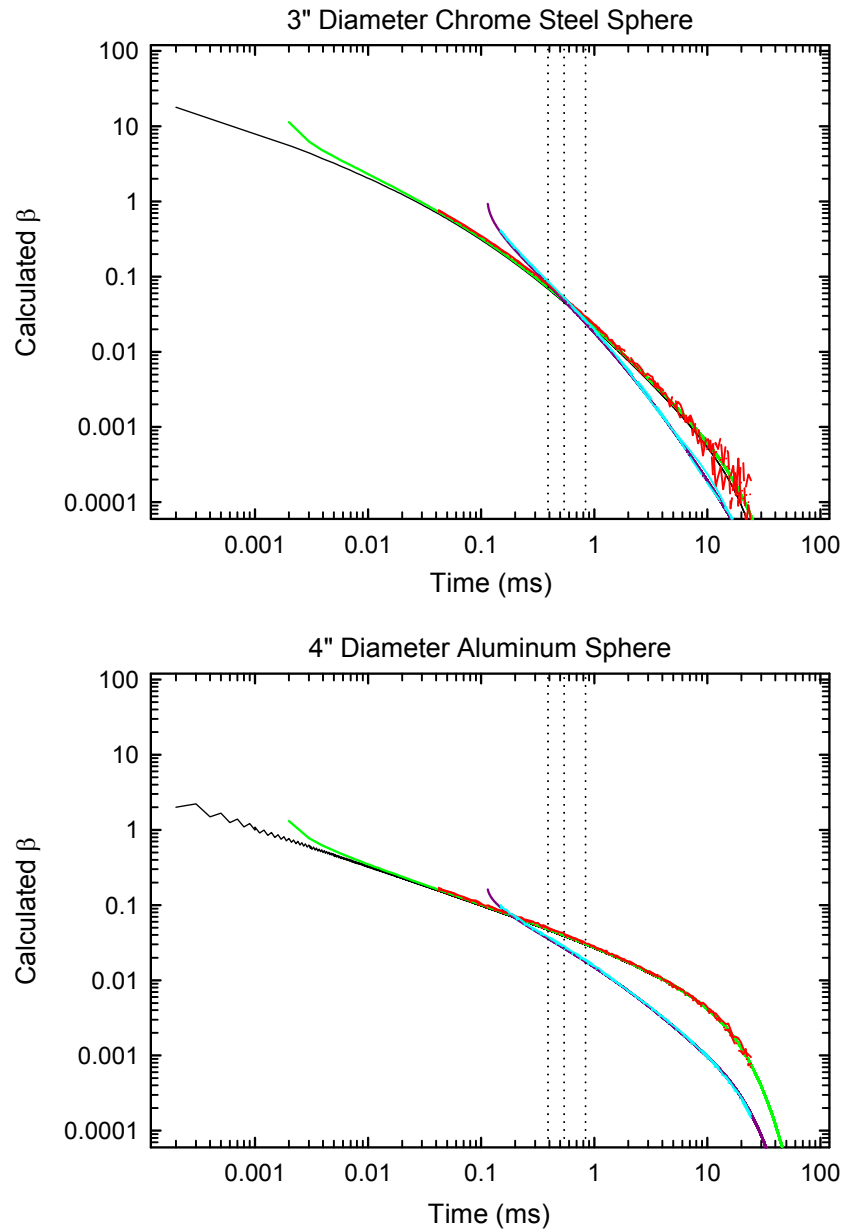


Figure 1 – Step response and effective β s for a 3" chrome steel and a 4" aluminum sphere. The underlying black curves represent the step response β s based on theory; the red curves represent the effective TEM array β s inverted from data; and the cyan curves represent the effective EM61-MK2 β s computed using the effective TEM array β s. The green and magenta curves represent the theoretical effective β s for the TEM array and the EM61-MK2, respectively. Please refer to the text for a full description of the method used. The vertical dotted lines represent the EM61-MK2 differential mode time gates.

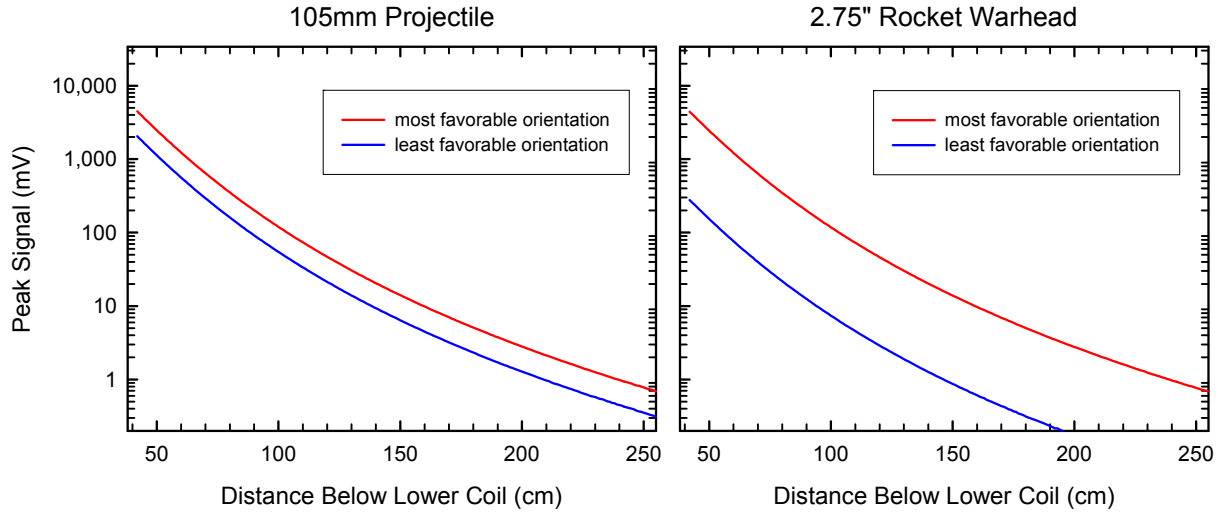


Figure 2 – Predicted EM61-MK2 signal at the second time gate as a function of depth for a 105-mm projectile (left) and a 2.75” rocket warhead (right). In both cases, the response to the object in its most favorable orientation is plotted as a red line and the least favorable orientation as a blue line.

For both items, the predicted response when the item is in its most favorable orientation (oriented vertically under the sensor) is plotted as a red line and that when the item is in its least favorable orientation (oriented horizontally under the sensor perpendicular to the sensor track) as a blue line. The length to diameter aspect ratio of the rocket warhead is substantially larger than that of the projectile accounting for the greater spread between the two responses in the left panel. The long axis of both targets is of similar size yielding similar responses in the most favorable orientation. Except in the most unfavorable conditions, site noise is typically 1 mV or below allowing both of these items to be detected at depths approaching 1 m under standard deployment conditions.

DATA COLLECTION PROCEDURES

Two data collections were carried out for each of the munitions items studied. Although the target response coefficients needed to predict the sensor signal as a function of depth can be determined from a series of EM61-MK2 measurements, it proved to be more efficient to determine the β s using our TEM array using the procedures outlined above. This instrument, developed with ESTCP support, comprises a five-by-five array of time-domain EM sensors each consisting of a 35-cm transmit coil and an inner 25-cm receive coil, Figure 3. With the munitions item to be investigated placed under the center sensor in the array, Figure 4, the transmit coils are energized sequentially and decay data are collected from all 25 receive coils; 625 individual decays in total, from 40 μ s to 25 ms after the primary is turned off.

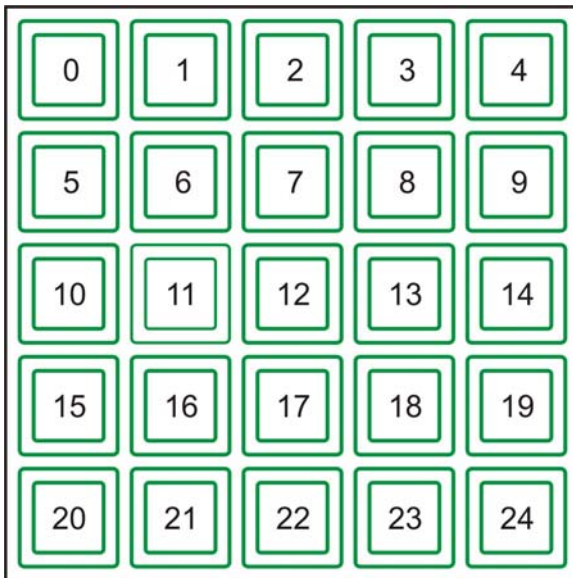


Figure 3 – Schematic of the 25-element TEM array used to determine the response coefficients of the test objects.



Figure 4 – 81-mm mortar placed under the TEM array. Sensors 21, 22, and 23 are visible.

A small subset of the data collected from a 2.75-in warhead oriented horizontally along track 35cm below the sensor array is shown in Figure 5. The nine decay curves shown are the response measured at the nine central receivers when the corresponding transmit coil is energized (monostatic response). Some of the shape information available from these sensors is evident in the plot. The decays measured using sensors 7 and 17, which primarily excite longitudinal modes of a prolate spheroidal target oriented along track, have distinct decay behavior from sensors 11 and 13, which primarily excite transverse modes.

TEM array data were collected from each object studied at different target orientations and for at least two array-object distances. These data were inverted for target response coefficients, β , as described above. Combined with the known transmit and receive properties of the EM61-MK2, these β s were used to predict the sensor response to each test item as a function of depth.

In order to validate these predictions, EM61-MK2 surveys were conducted over each of the test objects positioned at a variety of depths and orientations in our test pit at Blossom Point. These surveys consisted of a single pass of the sensor at normal survey speed over the object starting ten meters in front of the pit and continuing ten meters past the pit. Before and after each series of measurements, data were collected over the empty pit to ensure that the sensor background was at reasonable levels. The survey

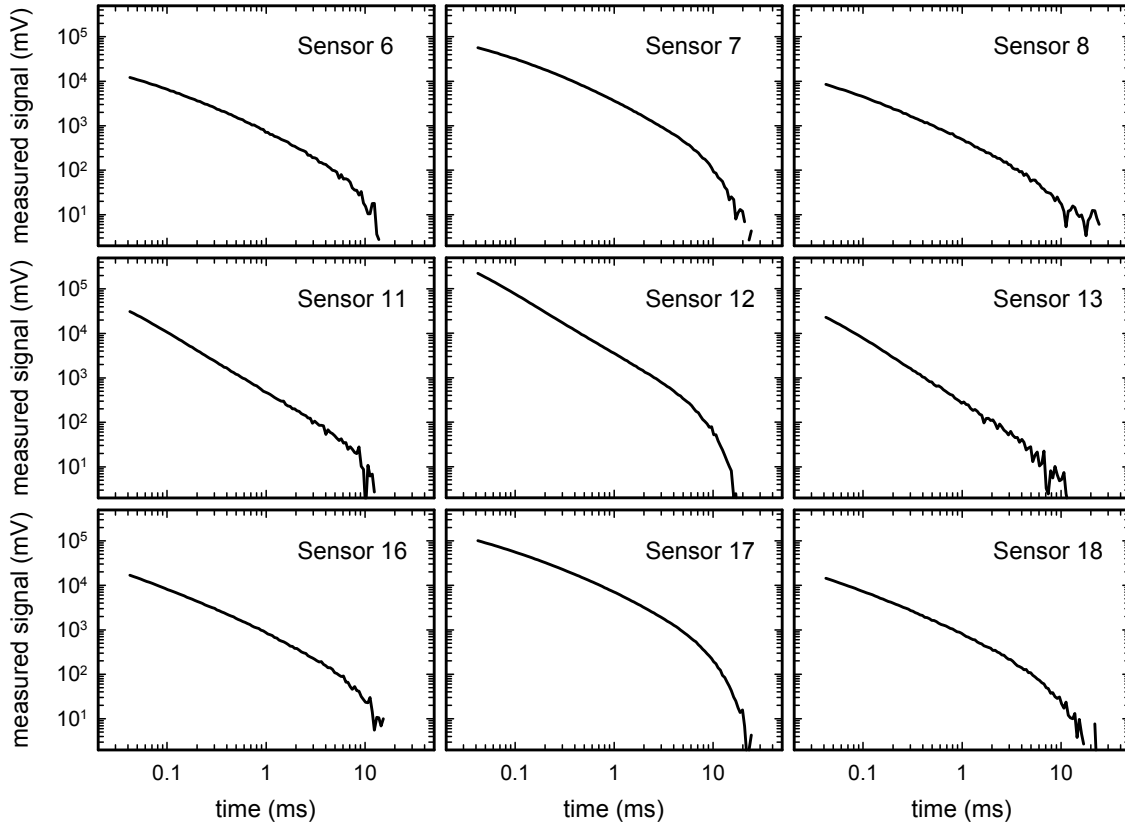


Figure 5 – Measured response of a 2.75-in warhead oriented horizontally along track 35 cm below the TEM array. The nine decays shown represent the response of the nine central receivers (see Figure 3) when the corresponding transmitter is energized.

data were background corrected using data collected before and after the test pit and the largest amplitude signal for each of the four time gates selected. In many cases this is not the measurement directly above the object; for a cylinder placed flat and oriented along the survey track, the peak signals are observed before and after the object. Each object was measured at nine to twelve unique positions.

For all EM61-MK2 data reported in this report, the sensor was operated in differential or “D” mode with three sampling gates devoted to the lower, primary receive coil and one devoted to the upper receive coil. The nominal delay time and receive coil for each of the four gates are listed in Table 1.

Table 1. Nominal delay time and receive coil used for each of the EM61-MK2 gates in “D” mode.

Gate	Receive Coil	Nominal Delay
1	Lower	390 μ s
2	Lower	540 μ s
3	Lower	840 μ s
4	Upper	840 μ s

RESULTS

The results of this investigation are shown in Figures 6 through 18. For each of the figures, the top panel is a photograph of the actual item measured and the bottom panel shows the predicted and measured EM61-MK2 response at the second time gate. The predicted response when the item is in its least favorable orientation is plotted as a solid blue line. Measured responses are plotted as crosses. In all cases, the measured responses are described well by the calculated curves. The system noise, which limits the ultimate depth of detection of the item under investigation, determined at the site is plotted as a dash-dot line. The RMS noise at this site was 0.5 mV for gate 2 but this is a strong function of the roughness of the terrain and may be higher at other sites. The observed static and moving RMS noise amplitudes for all gates are given in Table 2. Note that the noise on the upper coil (gate 4) increases dramatically in survey mode due to the extra motion of the upper coil.

Table 2. Measured RMS noise for each of the four gates in static and survey mode.

Gate	Static (mV)	Survey (mV)
1	0.5	0.8
2	0.1	0.5
3	0.2	0.3
4	0.3	1.3

A depth below the surface corresponding to 11x an objects diameter is often the *de facto* expectation for detectability with modern geophysical equipment. It is the signal at this depth, with a safety margin of 50%, which was used as an anomaly selection threshold in the ESTCP Classification Pilot Program [6]. The minimum signals predicted for all the targets investigated for all four gates for this 11x depth are tabulated in Table 3. All predicted sensor responses are tabulated in a spreadsheet which is attached electronically as Appendix A.

The test pit at Blossom Point is only a little deeper than 1-m. Thus, for the larger objects we were unable to make measurements down to this 11x depth. This has no practical effect as the predicted responses are well validated by the data collected down to 1 m.

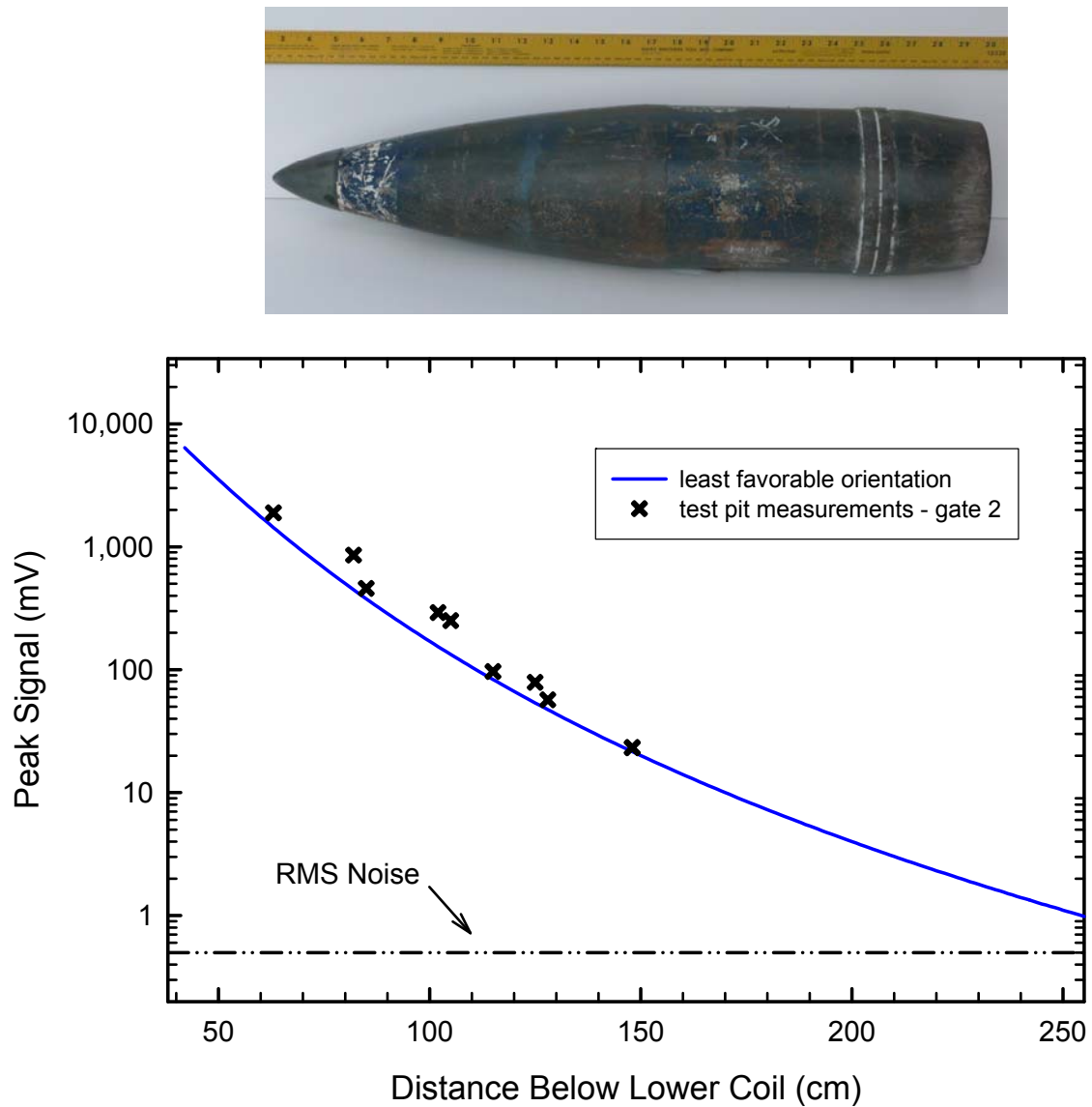


Figure 6 – EM61-MK2 signal at the second time gate as a function of the distance of the center of a 155-mm projectile below the sensor's bottom coil. The predicted response to the object in its least favorable orientation is shown as a solid line, test pit measurements are plotted as crosses, and the site noise is shown as a dot-dash line.

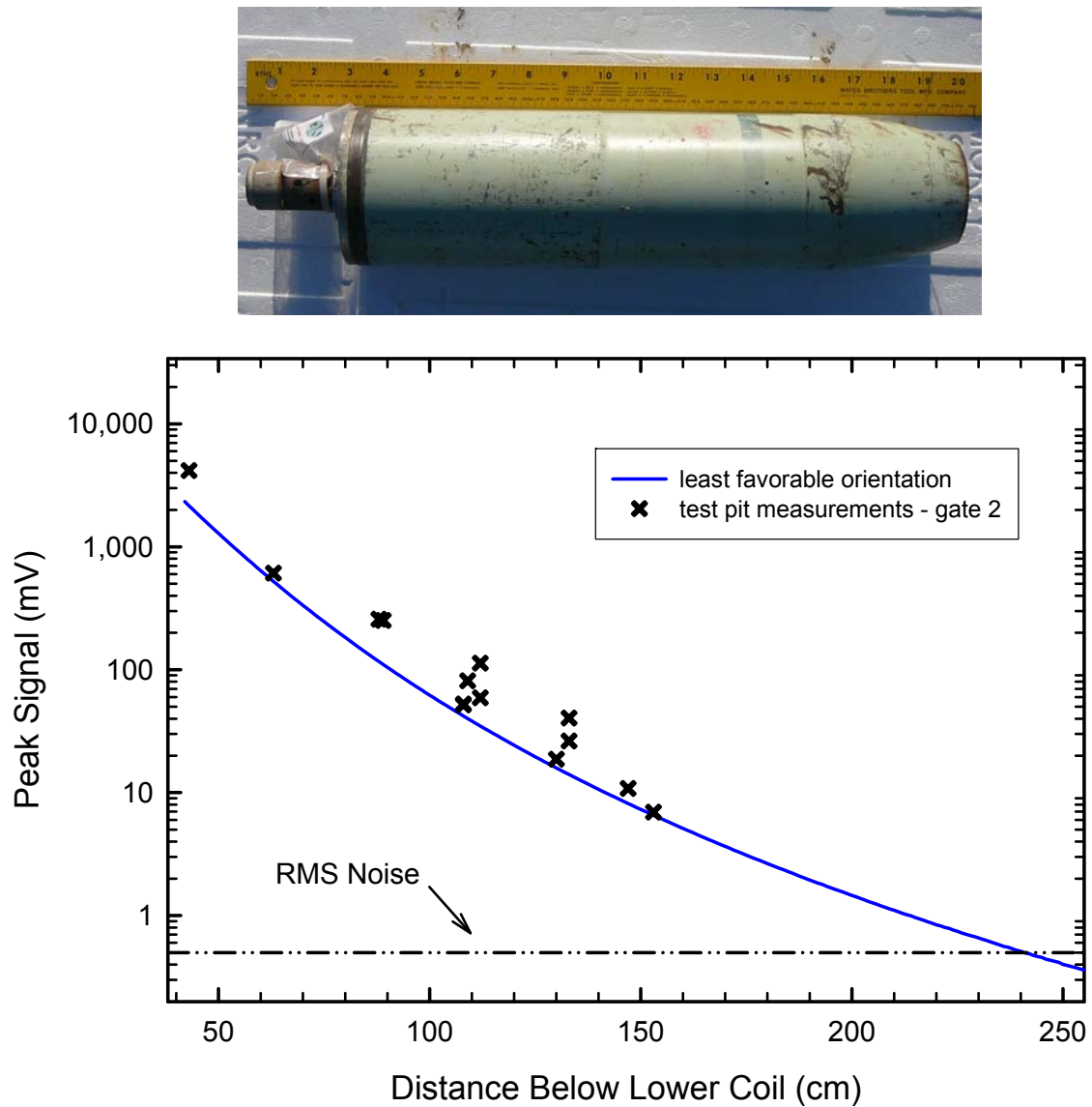


Figure 7 – EM61-MK2 signal at the second time gate as a function of the distance of the center of a 4.2-in mortar below the sensor's bottom coil. The predicted response to the object in its least favorable orientation is shown as a solid line, test pit measurements are plotted as crosses, and the site noise is shown as a dot-dash line.

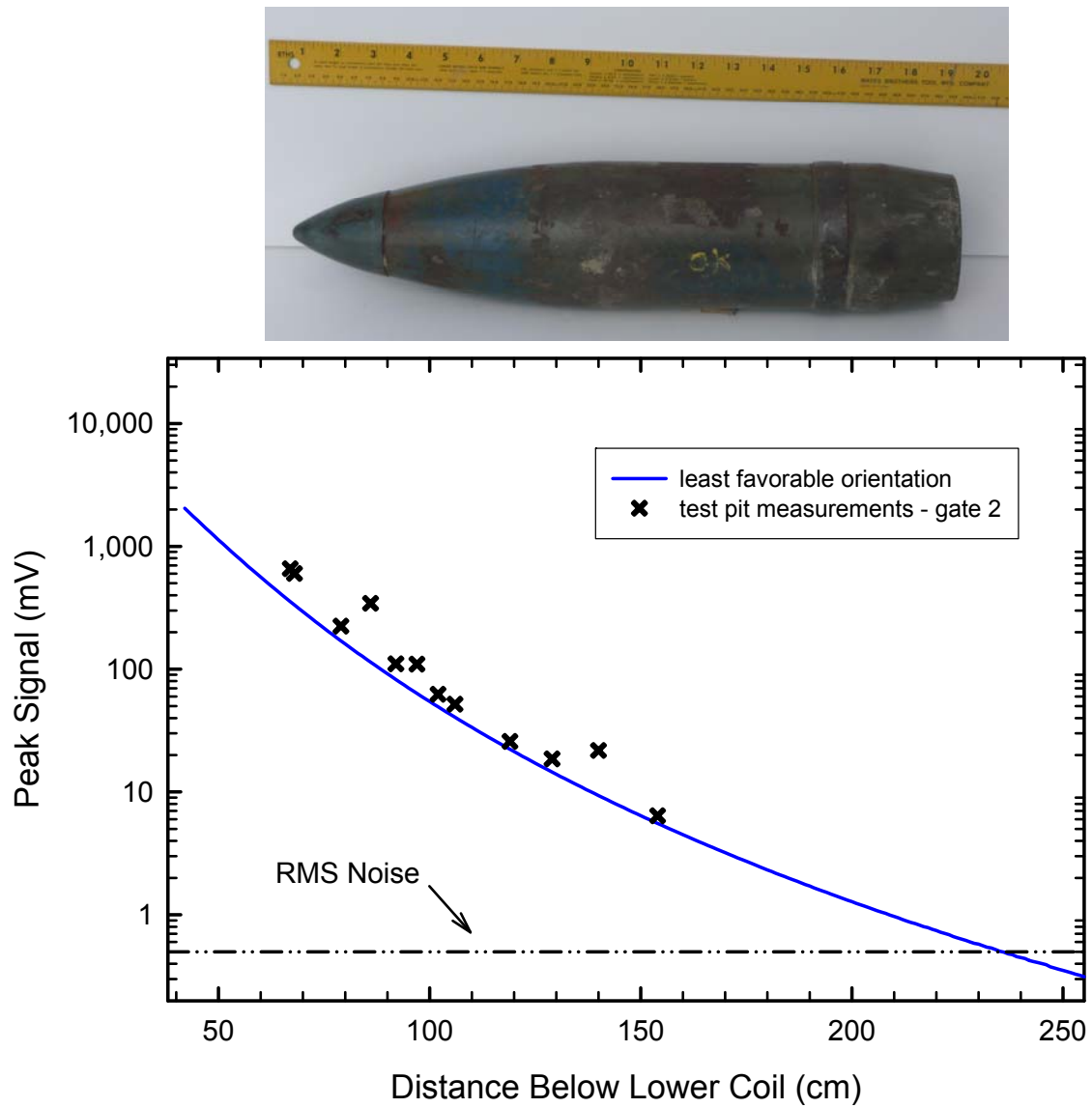


Figure 8 – EM61-MK2 signal at the second time gate as a function of the distance of the center of a 105-mm projectile below the sensor's bottom coil. The predicted response to the object in its least favorable orientation is shown as a solid line, test pit measurements are plotted as crosses, and the site noise is shown as a dot-dash line.

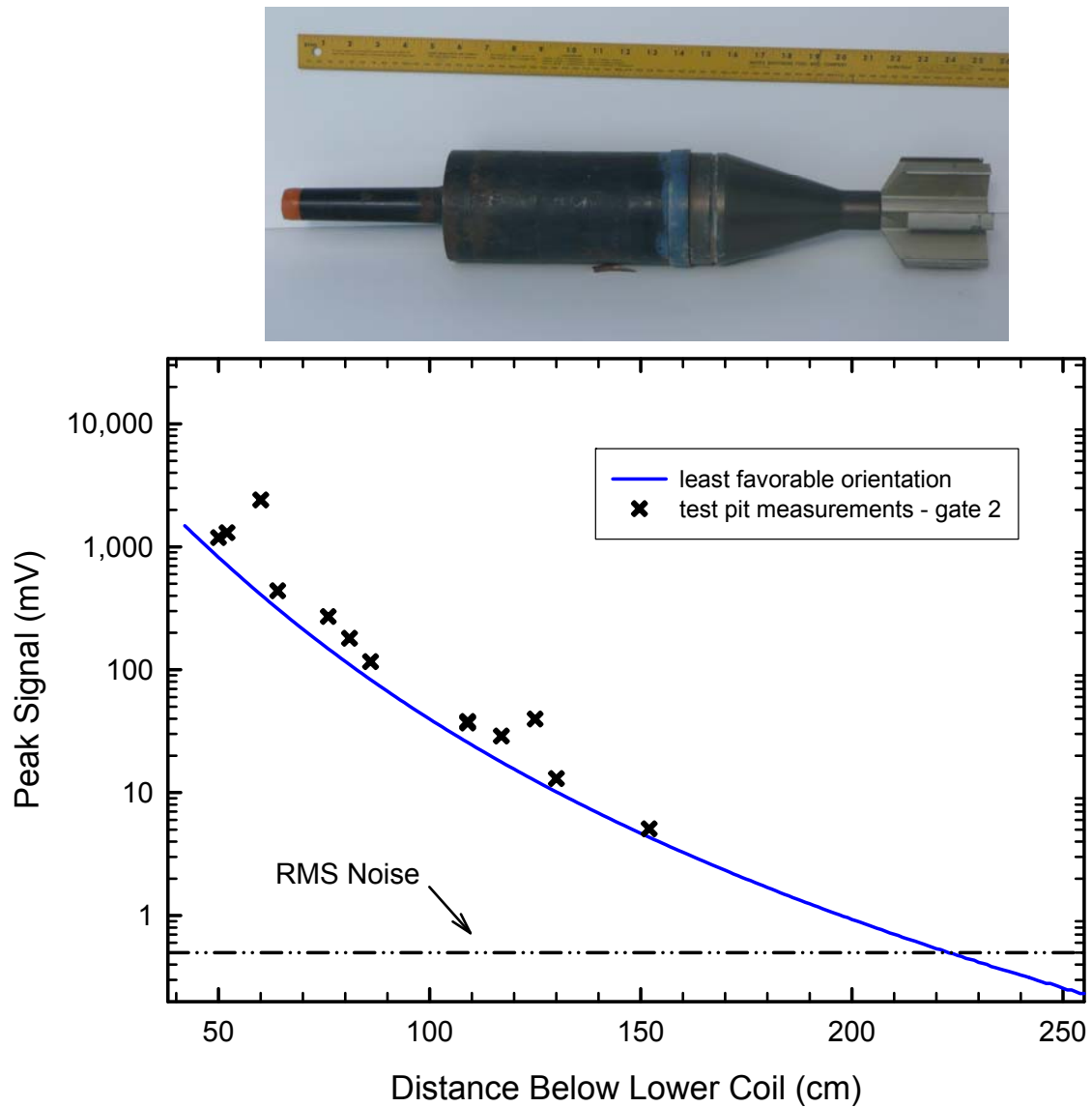


Figure 9 – EM61-MK2 signal at the second time gate as a function of the distance of the center of a 105-mm HEAT projectile below the sensor's bottom coil. The predicted response to the object in its least favorable orientation is shown as a solid line, test pit measurements are plotted as crosses, and the site noise is shown as a dot-dash line.

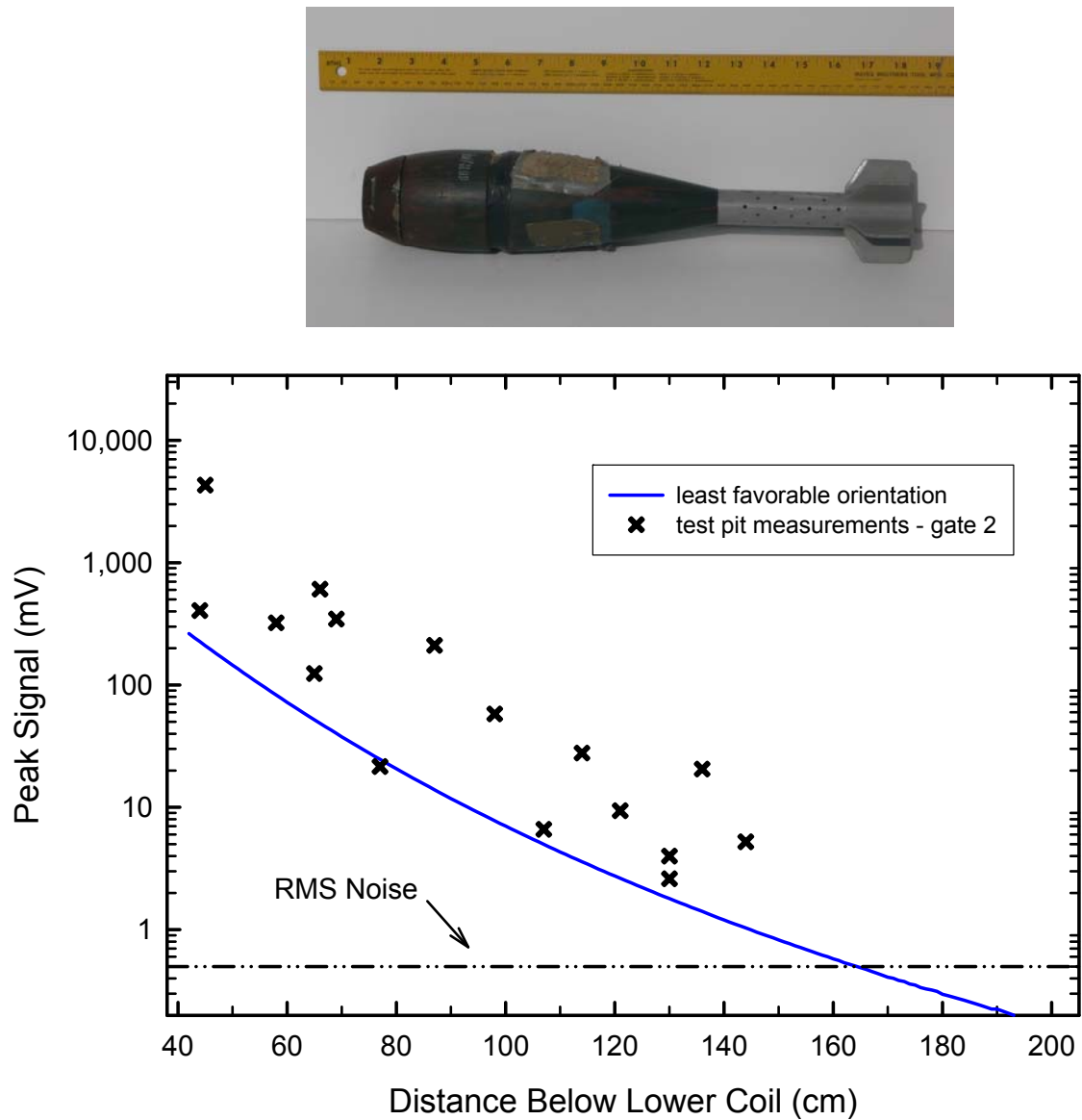


Figure 10 – EM61-MK2 signal at the second time gate as a function of the distance of the center of an 81-mm mortar below the sensor's bottom coil. The predicted response to the object in its least favorable orientation is shown as a solid line, test pit measurements are plotted as crosses, and the site noise is shown as a dot-dash line.

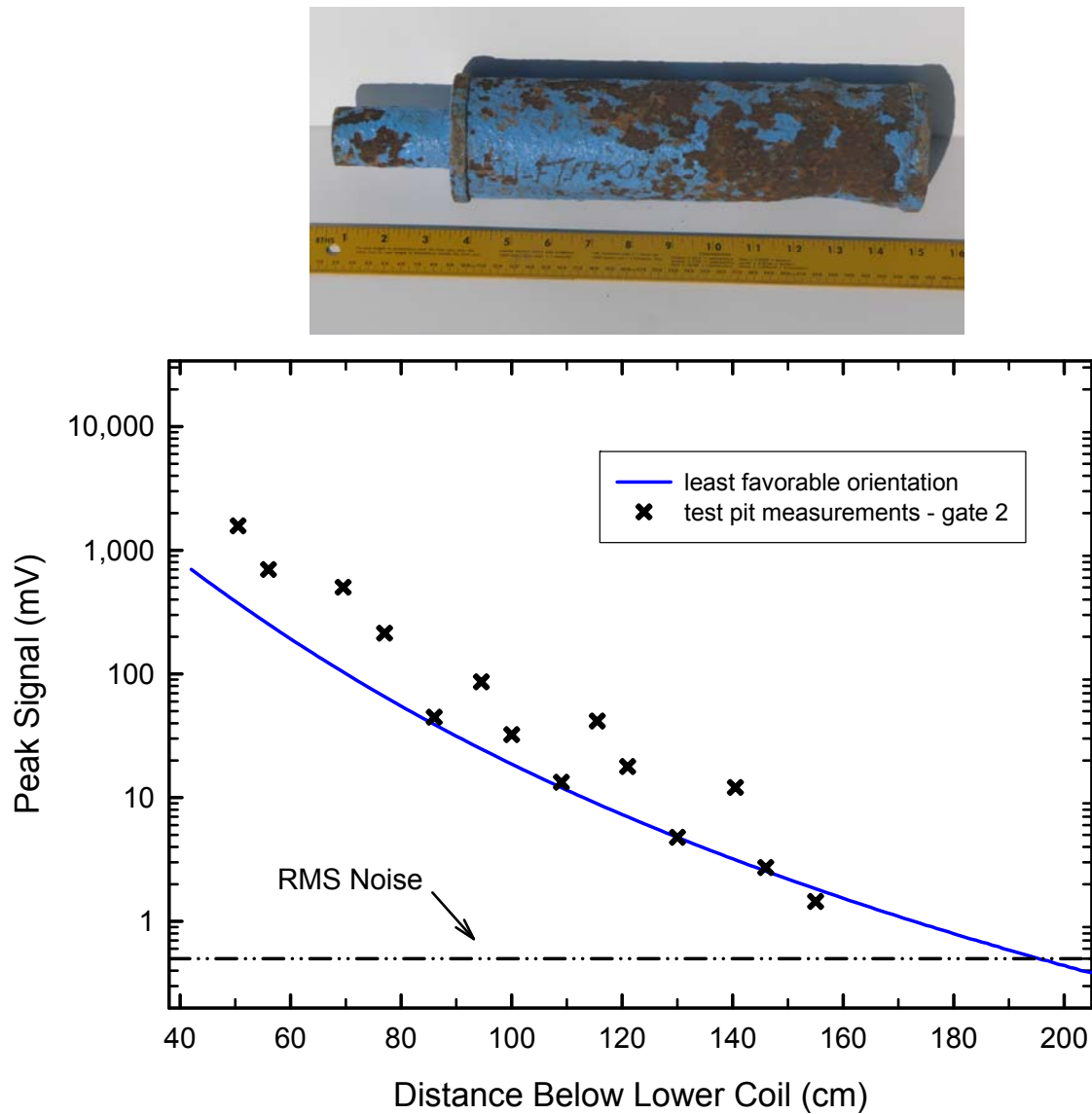


Figure 11 – EM61-MK2 signal at the second time gate as a function of the distance of the center of a 3-in Stokes mortar below the sensor's bottom coil. The predicted response to the object in its least favorable orientation is shown as a solid line, test pit measurements are plotted as crosses, and the site noise is shown as a dot-dash line.

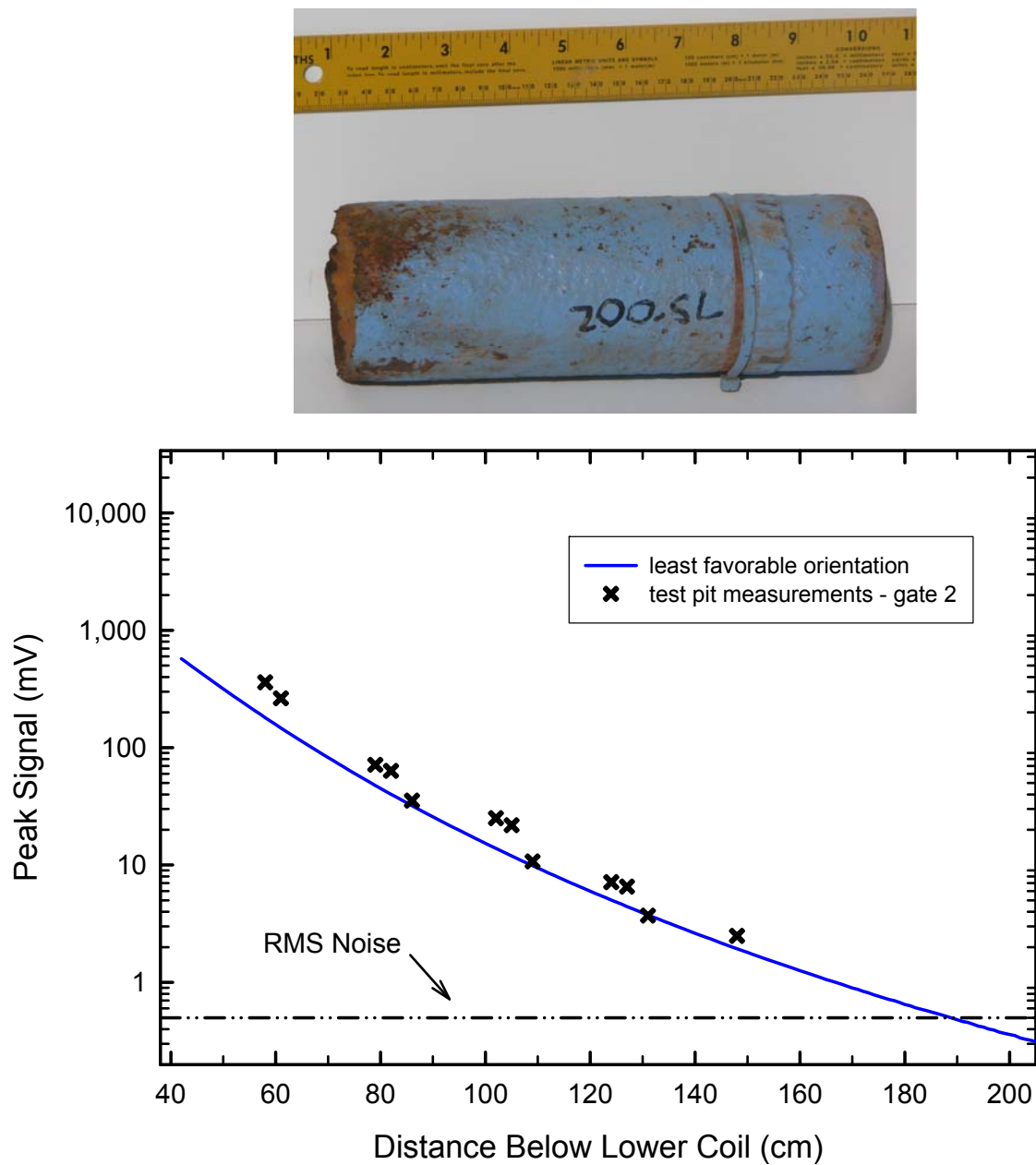


Figure 12 – EM61-MK2 signal at the second time gate as a function of the distance of the center of a 75-mm projectile below the sensor's bottom coil. The predicted response to the object in its least favorable orientation is shown as a solid line, test pit measurements are plotted as crosses, and the site noise is shown as a dot-dash line.

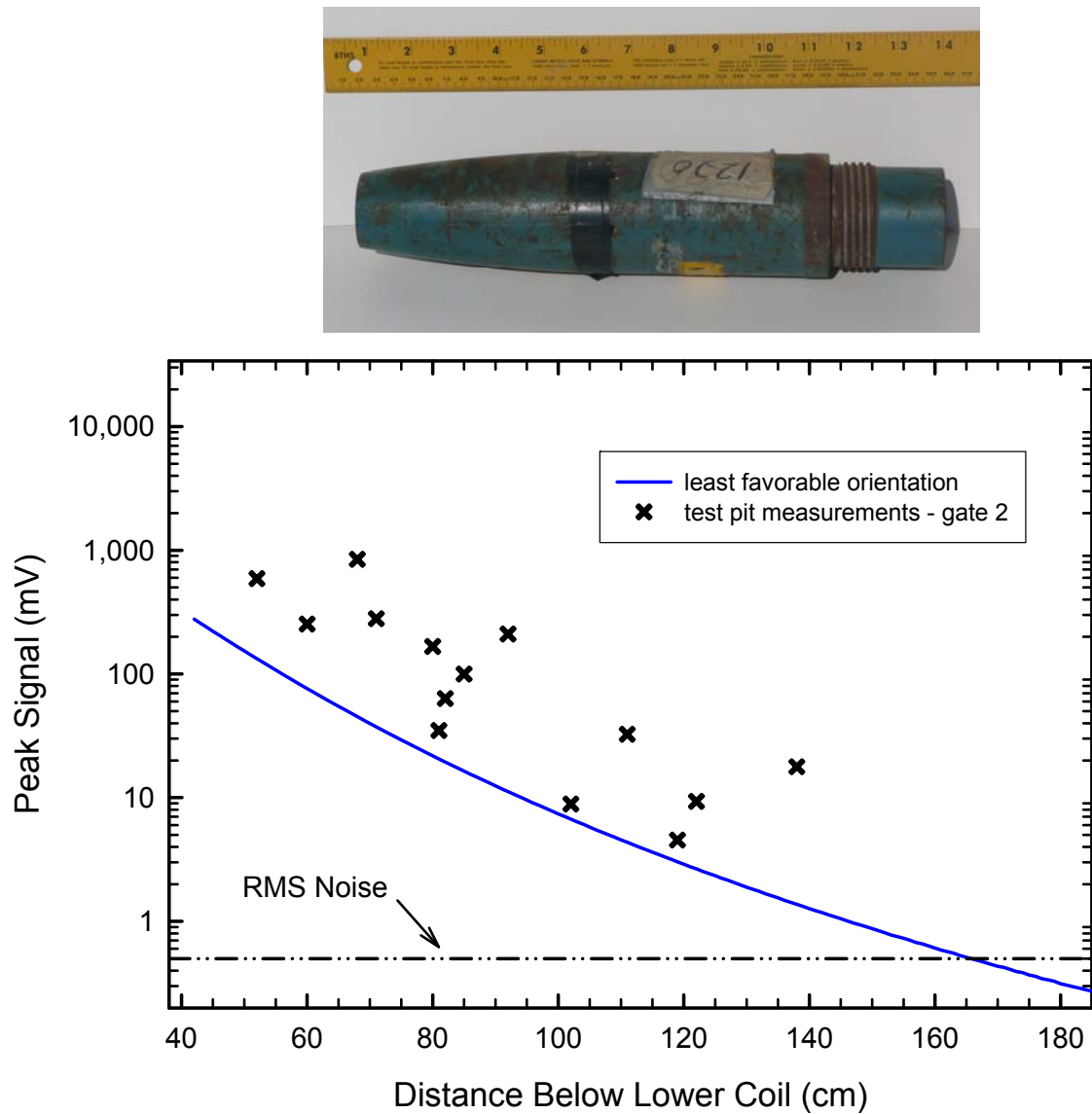


Figure 13 – EM61-MK2 signal at the second time gate as a function of the distance of the center of a 2.75-in rocket warhead below the sensor's bottom coil. The predicted response to the object in its least favorable orientation is shown as a solid line, test pit measurements are plotted as crosses, and the site noise is shown as a dot-dash line.

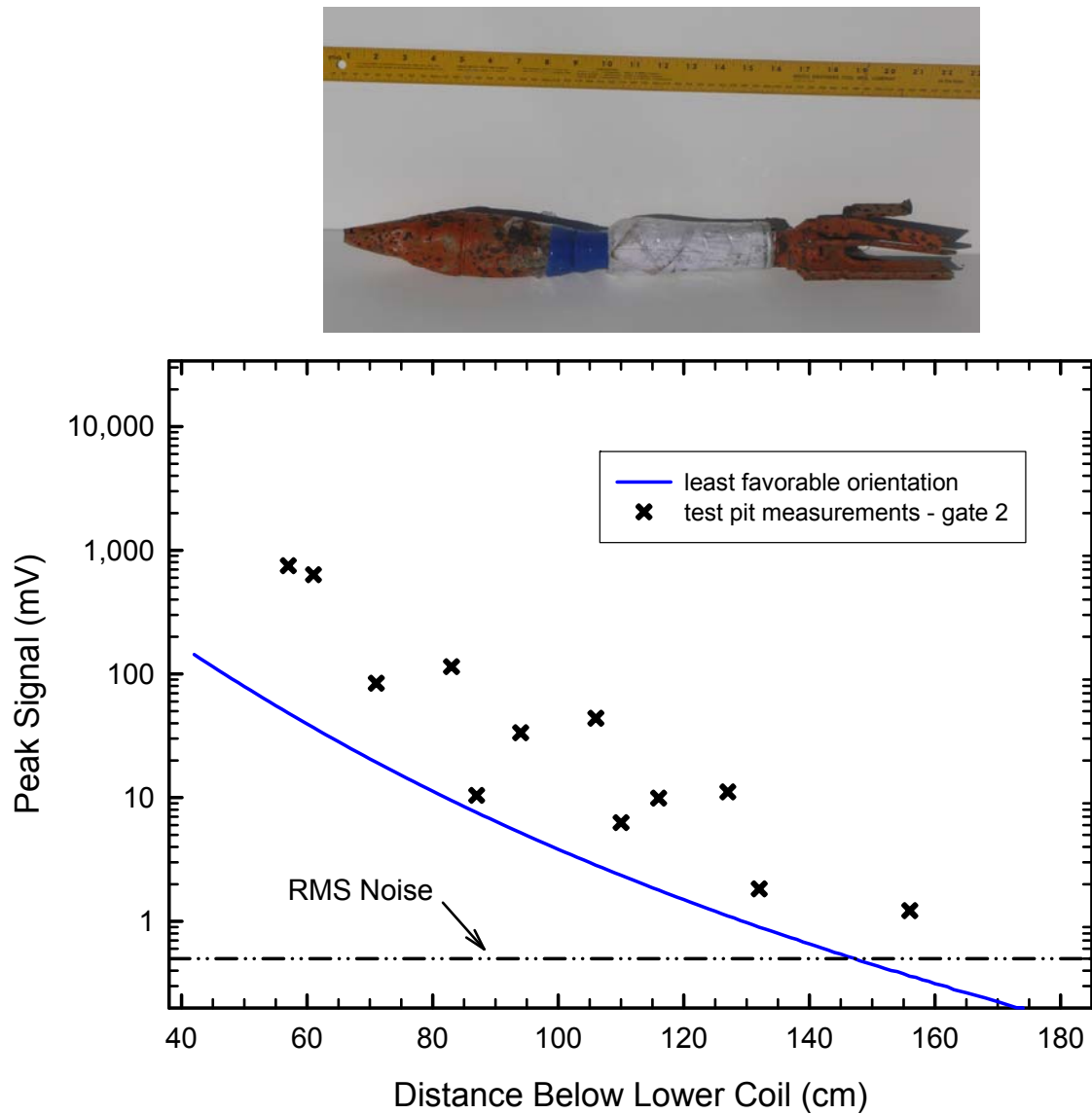


Figure 14 – EM61-MK2 signal at the second time gate as a function of the distance of the center of a 2.36-in Rocket Propelled Grenade below the sensor's bottom coil. The predicted response to the object in its least favorable orientation is shown as a solid line, test pit measurements are plotted as crosses, and the site noise is shown as a dot-dash line.

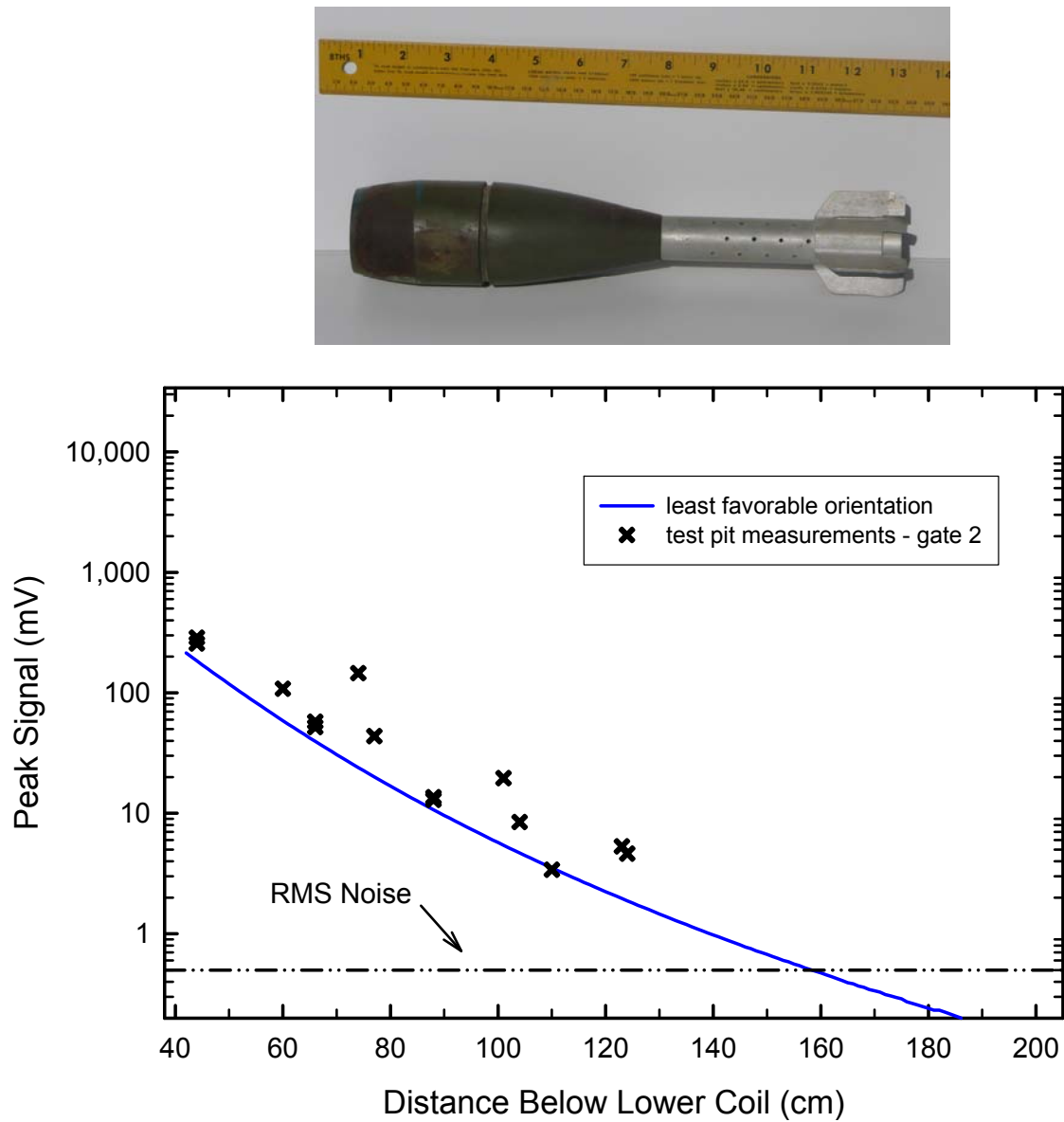


Figure 15 – EM61-MK2 signal at the second time gate as a function of the distance of the center of a 60-mm mortar below the sensor's bottom coil. The predicted response to the object in its least favorable orientation is shown as a solid line, test pit measurements are plotted as crosses, and the site noise is shown as a dot-dash line.

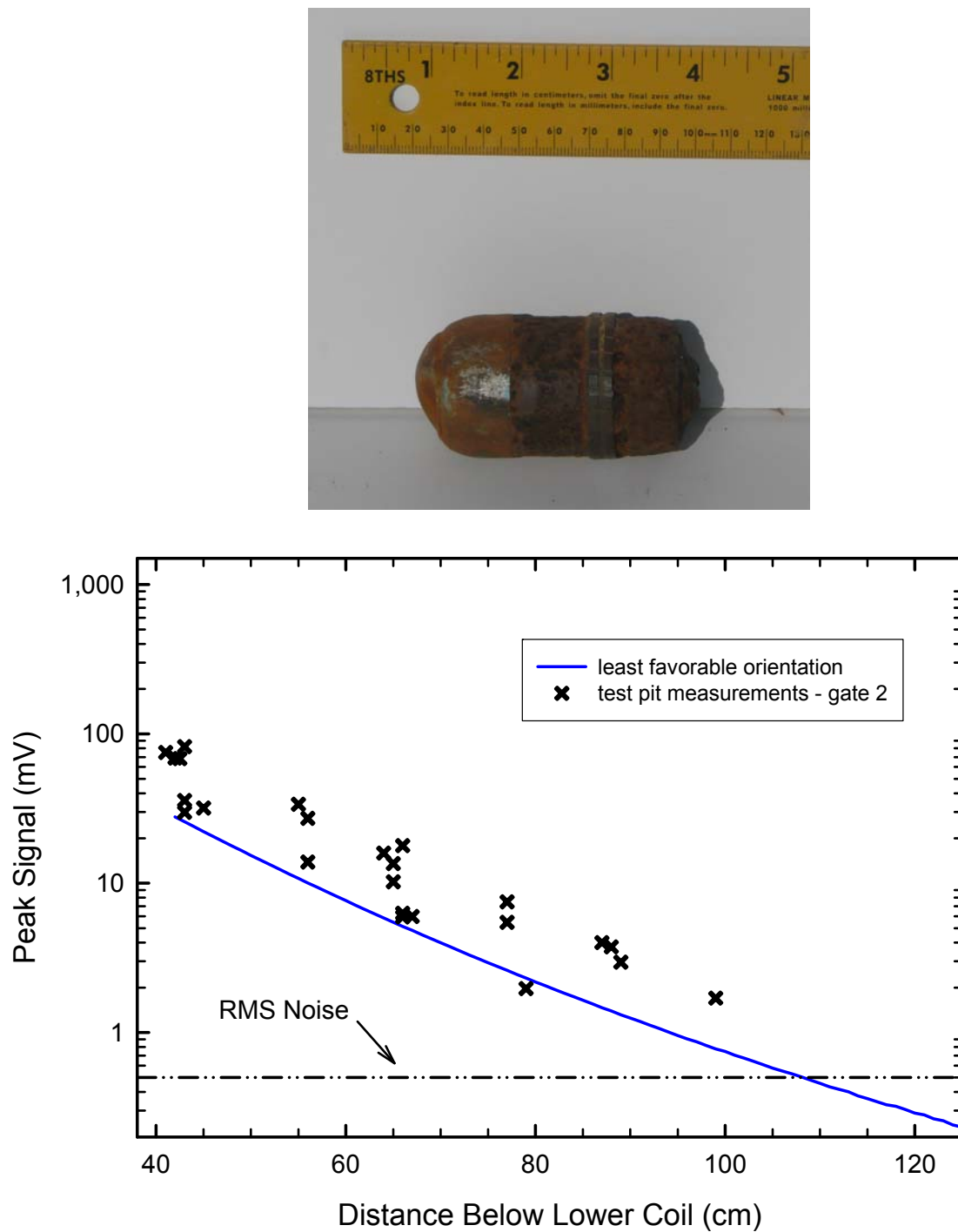


Figure 16 – EM61-MK2 signal at the second time gate as a function of the distance of the center of a 40-mm grenade below the sensor's bottom coil. The predicted response to the object in its least favorable orientation is shown as a solid line, test pit measurements are plotted as crosses, and the site noise is shown as a dot-dash line.

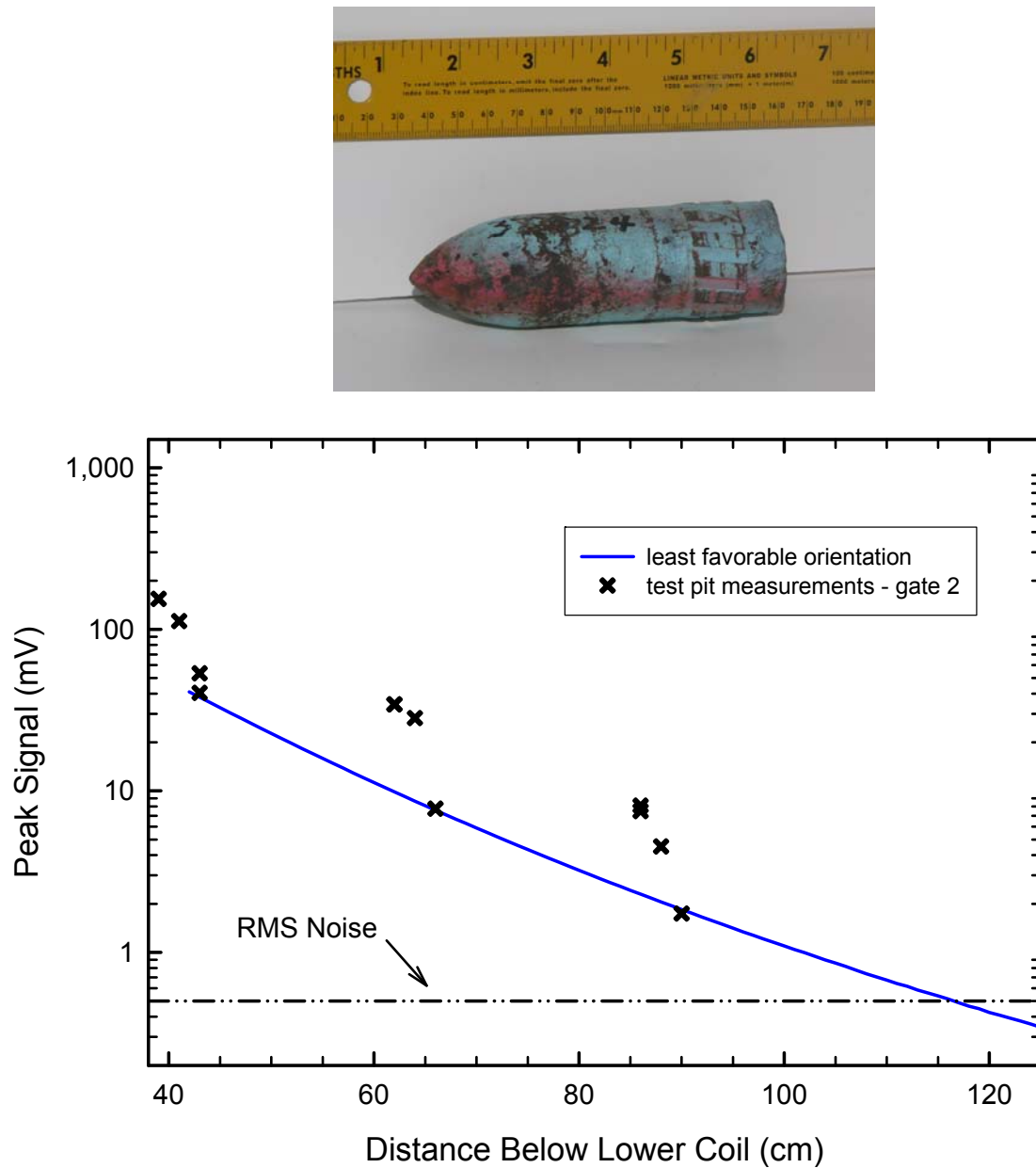


Figure 17 – EM61-MK2 signal at the second time gate as a function of the distance of the center of a 37-mm projectile below the sensor's bottom coil. The predicted response to the object in its least favorable orientation is shown as a solid line, test pit measurements are plotted as crosses, and the site noise is shown as a dot-dash line.

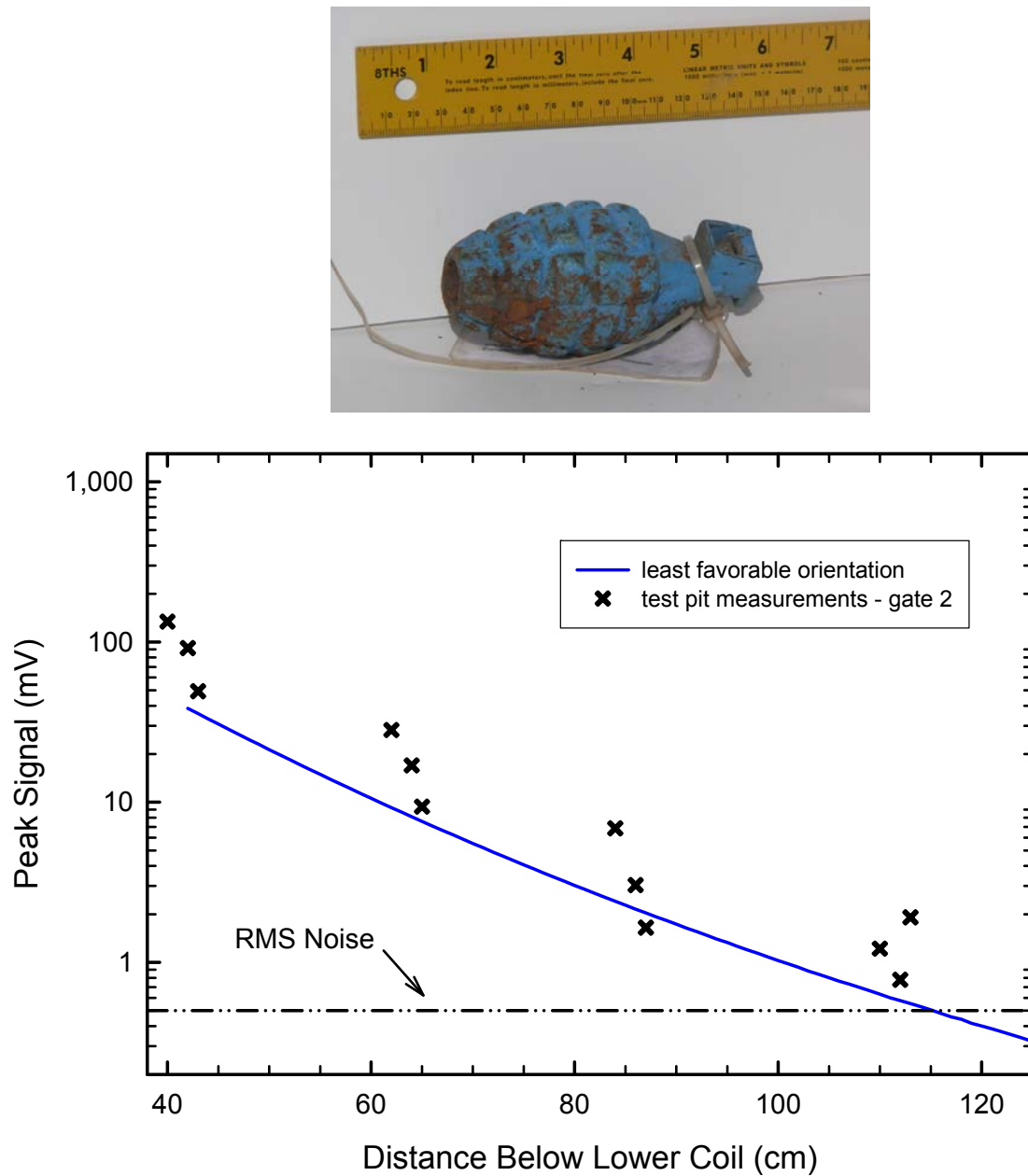


Figure 18 – EM61-MK2 signal at the second time gate as a function of the distance of the center of a hand grenade below the sensor’s bottom coil hand grenade. The predicted response to the object in its least favorable orientation is shown as a solid line, test pit measurements are plotted as crosses, and the site noise is shown as a dot-dash line.

Table 3. Predicted minimum EM61-MK2 signal for a variety of munitions at a depth corresponding to 11x their respective diameter. The sensor is assumed to be deployed on its standard wheels which correspond to the bottom coil 42 cm above the ground.

Item	11x Depth (m)	Minimum Signal at 11x Depth			
		Gate 1 (mV)	Gate 2 (mV)	Gate 3 (mV)	Gate 4 (D) (mV)
155-mm projectile	1.71	4.3	2.8	1.7	3.7
4.2-in mortar	1.17	8.8	5.3	3.0	5.9
105-mm projectile	1.16	8.0	4.9	2.8	5.5
105-mm HEAT projectile	1.16	5.8	3.6	2.0	3.9
81-mm mortar	0.89	3.1	1.7	0.9	1.6
3-in Stokes mortar	0.84	10.0	5.6	2.8	5.1
75-mm projectile	0.83	8.2	4.9	2.8	5.0
2.75-in rocket warhead	0.77	5.7	3.0	1.5	2.6
2.36-in rocket propelled grenade	0.66	4.9	2.6	1.3	2.2
60-mm mortar	0.66	6.5	3.9	2.2	3.7
40-mm grenade	0.44	2.8	1.6	0.7	1.1
37-mm projectile	0.41	5.1	2.7	1.3	1.9
hand grenade	0.61	1.7	0.9	0.4	0.7

SUMMARY

We have made use of the NRL TEM Array to characterize a number of inert munitions items commonly found on Military Munitions Response Sites. Using these data we have determined EM response coefficients for each object. These response coefficients have been used to calculate the expected signal from an EM61-MK2 over each object as a function of depth and orientation. These results have been presented graphically and the minimum signal expected at a depth corresponding to 11x the objects diameter has been tabulated.

REFERENCES

1. Harbaugh, G. R., Steinhurst, D. A., and Khadr, N. "MTADS Demonstration at Camp Sibert Magnetometer / EM61 MkII / GEM-3 Arrays," Demonstration Data Report, September 26, 2007.
2. Baum, C. (ed.), *Detection and Identification of Visually Obscured Targets*, Taylor and Francis, 1999.
3. Goldstein, H., *Classical Mechanics*, 2nd ed., Addison-Wesley, 1980.
4. Miller, J., and Furuya, T., "Variability of Real UXO," Symposium on the Application of Geophysics to Engineering and Environmental Problems 2007, Denver CO.
5. Miller, J., and Kingdon, J., "Quantification of UXO Variability for Target Discrimination," UXO Forum 2006, Las Vegas, NV.
6. Nelson, H. H., Kaye, K., and Andrews, A., "ESTCP Pilot Program, Classification Approaches in Munitions Response," ESTCP Web Site.